ABAQUS and ANSYS implementations of peridynamics-based finite element method (PeriFEM) for brittle fracture

Fei Han[a,*], Zhibin Li[a], Jianyu Zhang[a], Zhiying Liu[a], Chen Yao[a], Wenping Han[a]

[a]*State Key Laboratory of Structural Analysis for Industrial Equipment, Department of Engineering Mechanics, Dalian University of Technology, Dalian 116023, China*

Abstract

PeriFEM is a reformulation of traditional FEM for solving peridynamic equations numerically. It takes the non-local feature of peridynamics into account, and thus possesses the same computational framework as traditional FEM. Such advantages enable the convenient integration of peridynamics and commercial FEM software. Therefore, in the current work, we address the basics of PeriFEM within the framework of traditional FEM first, based on which, we propose a unified implementation technique for peridynamics in the commercial FEM software. And we implement the peridynamic simulation in ANSYS and ABAQUS, respectively. The implicit algorithm is used in both software, but different convergence criteria are adopted due to their own features. In ANSYS, APDL allows users to get the broken-bond information from UPFs conveniently, thus whether there are new broken bonds is adopted as the convergence criterion. In ABAQUS, it is not convenient for users to obtain the broken-bond information, thus the default convergence criterion in ABAQUS is used. The code that is integrated into ANSYS and ABAQUS are both verified through benchmark examples. The computational convergence and computational cost are compared. The results show that ABAQUS is more efficient, whereas the convergence criterion adopted in ANSYS is more robust. Finally, 3D examples are carried out to prove the ability of the proposed approach in dealing with complex engineering problems.

Keywords: PeriFEM, peridynamics, ANSYS, ABAQUS, damage and fracture

1. Introduction

Establishing mathematical models for natural phenomena is the second paradigm in the scientific investigation [1]. More specially, in the engineering and physics fields, many problems are traditionally summarized as a (group of) partial differential equation(s). However, the analytical solutions of those equations are usually difficult to obtain, thus we have to rely on numerical methods [2]. The finite element method (FEM) is one of the most popular numerical methods due to its standardization of the analysis process and applicability for a variety of problems.

*Corresponding author
Email address: hanfei@dlut.edu.cn (Fei Han)

However, the development of the FEM has not been smooth sailing, and it is said that even a well-known journal at that time shunned papers on the finite element method for many years [3]. In the 1960s, things turned around benefiting from Ed Wilson's liberal distribution of his first programs, making more and more people realize the value of FEM and devote themselves to this field. Then in the next few decades, numerous FEM software sprang up, which greatly promoted the application of FEM in engineering practice. In particular, commercial FEM software uses the interactive windows to make application more convenient and their appearance also makes the finite element analysis easier.

With the development of cutting-edge science and technologies, the service environment of engineering structure is getting more and more complicated, thus the analysis of them is facing new challenges, such as fracture. For this kind of problem, the traditional commercial FEM software seems a bit powerless. Faced with this situation, there are two strategies: 1) the developers integrate the advanced techniques into the software directly; 2) the users incorporate the advanced techniques with the software by the programmable interface. The first case may be more suitable for more mature technology because the development of software is expensive in terms of time and funding. The second case is more able to adapt to the most advanced techniques and accumulate experience for the first case. For example, before ABAQUS launched the version containing the extended finite element method (XFEM), Fang and Jin [4] had implemented the XFEM simulation in it. For other methods that have received widespread attention, there are also related work implemented in software, such as Lindgaard et al. [5] presented a cohesive zone finite element implemented with the user programmable feature (UPF) in ANSYS; Msekh et al [6], Molnár and Gravouil [7], Wu and Huang [8] incorporated the phase field model for fracture with ABAQUS by subroutines, just mention some examples.

Peridynamics also attracts many researchers' attention as a newborn non-local theory [9, 10]. The governing equations in peridynamics are integral-differential equations rather than partial differential equations, so discontinuities are naturally tolerated, which has great advantages in simulating fracture problems. Therefore, it will greatly promote engineering applications if the peridynamics could be incorporate commercial FEM software. However, due to the integration feature of peridynamic equations, only a few researchers use the element-based method to solve them [11, 12, 13], and most scholars use the particle-based method that directly approximates the integration as a Riemann summation [14, 15, 16], which is difficult to be compatible with the commercial FEM software. Therefore, to the best knowledge of the authors, there are only a few researchers who realized the peridynamics in commercial FEM software [17, 18, 19]. In the literature [17], Diyaroglu et al. used the truss element to present the peridynamic bond [20], thus the peridynamics simulation is implemented in ANSYS. In the literature [18], Huang et al. defined the collection of all peridynamic particles in a horizon as a new element and realized peridynamics simulation in ABAQUS. However, this type of element is undefined around the boundary, so a coupled model must be used. Bie et al. [19] overcame the aforementioned problems around the boundary and implemented dual peridynamics in ABAQUS, but have to define many types of elements. It is worth noting that, in the existing reports, although the peridynamics are implemented in the FEM software, they all use particles for

spatial discretization, and all for regular grids. So, element-based implementation of peridynamics in commercial FEM software is still lacking, especially with irregular meshes.

In this paper, we propose a unified implementation technique for peridynamics in the commercial FEM software based on the peridynamics-based finite element method (PeriFEM) [21, 22]. PeriFEM is an element-based method, and only two types of elements are needed. More importantly, the computational framework of PeriFEM is consistent with traditional FEM, thus it could be conveniently implemented in any commercial FEM software with a programmable interface. Therefore, we implemented the peridynamics simulation in ANSYS and ABAQUS based on PeriFEM, respectively, and it can be seen that the implementation process in these two software is similar, which means that PeriFEM can be easily extended to other commercial FEM software. In addition, two different convergence criteria for the implicit iteration are used in these two different software.

The rest of this paper is organized as follows: Section 2 reviews the basic formulations of the bond-based peridynamics. Section 3 introduces PeriFEM in detail, including the definition of elements, the shape functions, and the establishment of linear equations. Section 4 is devoted to the numerical algorithm of PeriFEM and two convergence criteria. Section 5 describes the implementation techniques of PeriFEM in ANSYS and ABAQUS. Numerical examples are displayed in Section 6 for verifying the algorithm and program. Finally, some conclusions are drawn in Section 7.

2. Review of peridynamics

Peridynamics is a reformulation of elasticity theory for discontinuities and long-range forces [9], which assumes that a point in the peridynamic continuum can interact with all the points in its neighborhood through the bond. According to the action mode of the force related to the bond, peridynamic formulations can be classified into bond-based peridynamics and state-based peridynamics [10]. Here we focus on the first one in the quasi-static case, and all "peridynamics" in subsequent sections refer to the bond-based peridynamics.

Like the classical elasticity theory, there are also three groups of basic equations in peridynamics, i.e., the equilibrium equations, the constitutive equations, and the kinematic equations, which are

$$\int_{H_{\delta(\boldsymbol{x})}} \boldsymbol{f}\left(\boldsymbol{\xi}\right) \mathrm{d}V_{\boldsymbol{\xi}} + \boldsymbol{b}(\boldsymbol{x}) = \boldsymbol{0}, \qquad \forall \boldsymbol{x} \in \Omega, \tag{1a}$$

$$\boldsymbol{f}\left(\boldsymbol{\xi}\right) = \boldsymbol{C}(\boldsymbol{\xi}) \cdot \boldsymbol{\eta}(\boldsymbol{\xi}), \qquad \forall \boldsymbol{x}' \in H_{\delta(\boldsymbol{x})}, \boldsymbol{x} \in \Omega, \tag{1b}$$

$$\boldsymbol{\eta}(\boldsymbol{\xi}) = \boldsymbol{u}(\boldsymbol{x}') - \boldsymbol{u}(\boldsymbol{x}), \qquad \forall \boldsymbol{x}', \boldsymbol{x} \in \Omega, \tag{1c}$$

respectively. Where $\Omega \subset \mathbb{R}^d$ $(d = 1, 2, 3)$ is the reference configuration, $\boldsymbol{x}$ and $\boldsymbol{x}'$ are points in Ω, $H_{\delta(\boldsymbol{x})}$ is the neighborhood of point $\boldsymbol{x}$ with a cut-off radius δ, $\boldsymbol{b}(\boldsymbol{x})$ is the external body force, $\boldsymbol{\xi} = \boldsymbol{x}' - \boldsymbol{x}$ is a relative position vector referred to as a bond, $\boldsymbol{\eta}(\boldsymbol{\xi})$ and $\boldsymbol{f}(\boldsymbol{\xi})$ are the measure of deformation and the pairwise force vector of bond $\boldsymbol{\xi}$, respectively. Supplemented to the basic equations, there are displacement boundary conditions in peridynamics, which reads

$$\boldsymbol{u}(\boldsymbol{x}) = \boldsymbol{u}^*(\boldsymbol{x}), \quad \forall \boldsymbol{x} \in \partial\Omega_{\boldsymbol{u}}, \tag{2}$$

where $\partial\Omega_{\boldsymbol{u}}$ refers to a part of the boundary of Ω where prescribed displacement is applied. Besides, note that the traction boundary conditions are not considered directly in the peridynamics [23].

$\boldsymbol{C}(\boldsymbol{\xi})$ in Eq. (1b) is the micro-modulus tensor, which is defined as [9]

$$\boldsymbol{C}(\boldsymbol{\xi}) = c(\boldsymbol{\xi})\boldsymbol{\xi} \otimes \boldsymbol{\xi}, \tag{3}$$

where $c(\boldsymbol{\xi})$ is the micro-modulus coefficient. Furthermore, $c(\boldsymbol{\xi})$ can be a multiplicative decomposed into the bond length related part $\hat{c}(\|\boldsymbol{\xi}\|)$ and disrelated part $\tilde{c}(\theta, \varphi)$ (where θ and φ are the polar angle and the azimuthal angle of $\boldsymbol{\xi}$ under the spherical coordinate system, respectively), i.e.,

$$c(\boldsymbol{\xi}) = \hat{c}(\|\boldsymbol{\xi}\|)\tilde{c}(\theta, \varphi), \tag{4}$$

where $\hat{c}(\|\boldsymbol{\xi}\|)$ could be a function of $\|\boldsymbol{\xi}\|$ in the form of constant (e.g., $\hat{c}(\|\boldsymbol{\xi}\|) = 1$ [15]), linear (e.g., $\hat{c}(\|\boldsymbol{\xi}\|) = 1 - \|\boldsymbol{\xi}\| / \delta$ [24]), or exponential (e.g., $\hat{c}(\|\boldsymbol{\xi}\|) = e^{-\|\boldsymbol{\xi}\|/l}$ [25], where l is a characteristic length related to the fracture process zone, see [26]), etc. Here we adopt the exponential function. $\tilde{c}(\theta, \varphi)$ could be determined according to the deformation energy equivalence between the peridynamics and the classical continuum mechanics. For isotropic materials, $\tilde{c}(\theta, \varphi)$ degenerates to a constant $\tilde{c}^0$ that related to Young's modulus E, i.e.,

$$\tilde{c}(\theta, \varphi) = \tilde{c}^0 = \begin{cases} \frac{3E}{\pi \int_0^\delta r^6 e^{-r/l} \mathrm{d}r}, & \text{for } d = 3, \\ \frac{3E}{\pi \int_0^\delta r^5 e^{-r/l} \mathrm{d}r}, & \text{for } d = 2 \text{ and plane-stress}, \\ \frac{16E}{5\pi \int_0^\delta r^5 e^{-r/l} \mathrm{d}r}, & \text{for } d = 2 \text{ and plane-strain}, \\ \frac{E}{\int_0^\delta r^4 e^{-r/l} dr}, & \text{for } d = 1. \end{cases} \tag{5}$$

For anisotropic materials, the calculation of $\tilde{c}(\theta, \varphi)$ is presented in Appendix A.

When the material failure needs to be considered, the simplest way is to allow the bonds to break. Here, we use the criterion proposed in [15] to introduce the material failure into the constitutive equation. The criterion is

$$\mu(\boldsymbol{\xi}, t) = \begin{cases} 1, & \text{if } s\left(\boldsymbol{\xi}, \tau\right) < s_{crit} \text{ for all } 0 \leq \tau \leq t, \\ 0, & \text{otherwise }, \end{cases} \tag{6}$$

where t and τ denote computational steps, μ is a history-dependent scalar-valued function that records whether $\boldsymbol{\xi}$ is broken, $s = \frac{\|\boldsymbol{\xi}+\boldsymbol{\eta}\|-\|\boldsymbol{\xi}\|}{\|\boldsymbol{\xi}\|}$ is the bond stretch, and s_{crit} is the critical bond stretch, which is generally considered to be related to the critical energy release rate [15, 27]. Multiply $\mu(\boldsymbol{\xi}, t)$ to the right-hand side of Eq. (3), and then the constitutive equation including bond break is obtained (see [15, Eq. (18)]). Based on the broken bonds, one can define the effective damage for each point $\boldsymbol{x}$ as [15]

$$\phi(\boldsymbol{x}) = \frac{\int_{H_\delta(\boldsymbol{x})} (1 - \mu(\boldsymbol{\xi}, t)) \mathrm{d}V_\xi}{\int_{H_\delta(\boldsymbol{x})} \mathrm{d}V_\xi}, \tag{7}$$

to indicate the macro-scope crack paths.

3. The peridynamics-based finite element method (PeriFEM)

The standardization of the analysis process is one of the significant features of the finite element method, which is also one of the important reasons why it is widely used in engineering analysis. In our previous papers, we derived the linear equations of PeriFEM based on the principle of minimum potential energy [21] and the principle of virtual work [22], respectively. In the present research, we will show the general steps of PeriFEM based on the general steps of the FEM as described in [2]. And the reader will find that the computational framework of PeriFEM is consistent with FEM, which enables the implementation of PeriFEM in FEM software.

3.1. Discretize and select the element types

This section is devoted to the spatial discretization and the definition of elements in PeriFEM. In this method, there are two types of elements. One is the *local element* for local quantities, such as body force, and the other is the *peridynamic element* (non-local element) for non-local quantities, such as peridynamic long-range force.

The definition of local elements is a generalization of the *finite element* in FEM. In FEM, a configuration Ω is divided into a finite number of elements, $\{e_i\}_{i=1}^m$, i.e., $\Omega = \bigcup_{i=1}^m e_i$ with m the element number, these elements are non-overlapping but share common edges and nodes between adjacent elements. The element that satisfies the above definitions is called the finite element. In PeriFEM, the configuration Ω is also discretized by a finite number of elements, i.e., $\Omega = \bigcup_{i=1}^m e_i$, these elements are also non-overlapping, but they do not have to share edge or node. In other words, the only difference between the local element and the finite element is that the former has no requirement on whether nodes and edges are shared between adjacent elements. Therefore, any type of finite element in FEM could be generalized to the local element and applied in PeriFEM.

The definition of peridynamic elements is based on the local elements. In brief, a peridynamic element is composed of two local elements, as shown in Fig. 1 (Note that the local elements are not limited to quadrilaterals for 2D and hexahedrons for 3D). In detail, for any two local elements, denoted as e_i and e_j, if they can interact with each other within the peridynamic horizon δ, then a peridynamic element denoted as $\bar{e}_k$ will be generated from them. In more detail, suppose the nodes of e_i and e_j are $\left[\mathrm{P}_{i_1}, \mathrm{P}_{i_2}, \cdots, \mathrm{P}_{i_{n_i}}\right]$ and $\left[\mathrm{P}_{j_1}, \mathrm{P}_{j_2}, \cdots, \mathrm{P}_{j_{n_j}}\right]$, respectively, where $\mathrm{P}_{\alpha_\beta}$ $(\alpha = i, j; \beta = 1, 2, \cdots, n_\alpha) \in \{\mathrm{P}_l\}_{l=1}^n$, which are the global nodes of Ω after discretized by local elements $\{e_i\}_{i=1}^m$. Then the nodes of $\bar{e}_k$ is $\left[\mathrm{P}_{k_1}, \mathrm{P}_{k_2}, \cdots, \mathrm{P}_{k_{\bar{n}_k}}\right] = \left[\mathrm{P}_{j_1}, \mathrm{P}_{j_2}, \cdots, \mathrm{P}_{j_{n_j}}, \mathrm{P}_{i_1}, \mathrm{P}_{i_2}, \cdots, \mathrm{P}_{i_{n_i}}\right]$, where $\bar{n}_k = n_j + n_i$. Finally, a set of peridynamic elements $\{\bar{e}_k\}_{k=1}^{\bar{m}}$ will be generated, where $\bar{m}$ denotes the number of peridynamic elements.

3.2. Select a displacement function

Now we introduce the approximation technique of element displacement. Such technique for the local element is similar to it in FEM, whereas for peridynamic is based on the approximation for the local element.

For any local element e_i, the displacements within it could be approximated based on the interpolation technique as

$$\boldsymbol{u}_i(\boldsymbol{x}) = \boldsymbol{N}_i(\boldsymbol{x})\boldsymbol{d}_i, \tag{8}$$

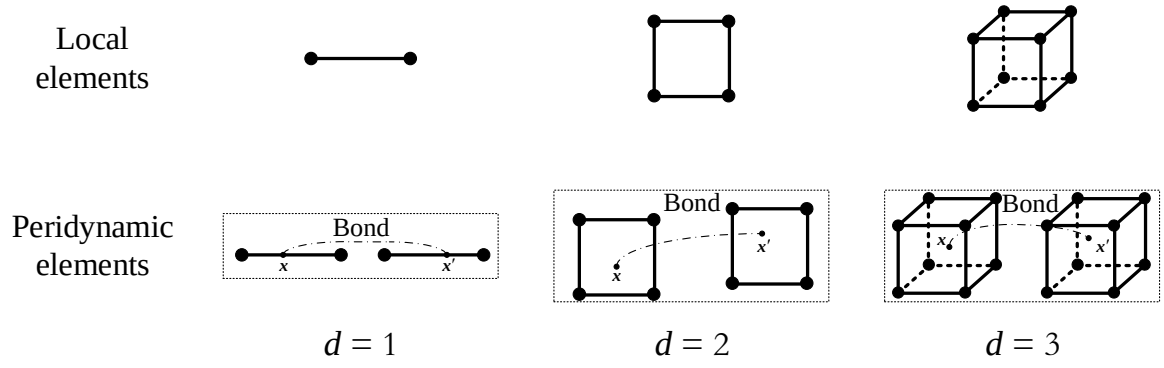

Figure 1: Schematic of the local elements and peridynamic elements.

where $\boldsymbol{N}_i(x)$ and $\boldsymbol{d}_i$ are respectively the local shape function matrix and the local nodal displacement vector of e_i, which are defined as

$$\boldsymbol{N}_i(\boldsymbol{x}) = \begin{bmatrix} N_{i_1}(\boldsymbol{x}) & 0 & 0 & N_{i_2}(\boldsymbol{x}) & 0 & 0 & \cdots & N_{i_{n_i}}(\boldsymbol{x}) & 0 & 0 \\ 0 & N_{i_1}(\boldsymbol{x}) & 0 & 0 & N_{i_2}(\boldsymbol{x}) & 0 & \cdots & 0 & N_{i_{n_i}}(\boldsymbol{x}) & 0 \\ 0 & 0 & N_{i_1}(\boldsymbol{x}) & 0 & 0 & N_{i_2}(\boldsymbol{x}) & \cdots & 0 & 0 & N_{i_{n_i}}(\boldsymbol{x}) \end{bmatrix}, \tag{9}$$

$$\boldsymbol{d}_i = \begin{bmatrix} u_{i_1} & v_{i_1} & w_{i_1} & u_{i_2} & v_{i_2} & w_{i_2} & \cdots & u_{n_i} & v_{n_i} & w_{n_i} \end{bmatrix}^T, \tag{10}$$

where N_{i_l} $(l = 1, 2, \cdots, n_i)$ is the shape function of node P_{i_l}, $u_{i_l}, v_{i_l}, w_{i_l}$ denote the X, Y, Z displacements of the node P_{i_l}, respectively.

For any peridynamic element $\bar{e}_k$, supposing it is generated from the local elements e_i and e_j, then the displacements within $\bar{e}_k$ could be approximated as

$$\bar{\boldsymbol{u}}_k(\boldsymbol{x}', \boldsymbol{x}) = \begin{bmatrix} \boldsymbol{u}_j(\boldsymbol{x}') \\ \boldsymbol{u}_i(\boldsymbol{x}) \end{bmatrix} = \bar{\boldsymbol{N}}_k(\boldsymbol{x}', \boldsymbol{x})\, \bar{\boldsymbol{d}}_k, \tag{11}$$

where

$$\bar{\boldsymbol{N}}_k(\boldsymbol{x}', \boldsymbol{x}) = \begin{bmatrix} \boldsymbol{N}_j(\boldsymbol{x}') & \boldsymbol{0} \\ \boldsymbol{0} & \boldsymbol{N}_i(\boldsymbol{x}) \end{bmatrix}, \tag{12}$$

$$\bar{\boldsymbol{d}}_k = \begin{bmatrix} \boldsymbol{d}_j \\ \boldsymbol{d}_i \end{bmatrix}, \tag{13}$$

are the peridynamic shape function matrix and the peridynamic nodal displacement vector of $\bar{e}_k$, respectively.

3.3. The force/deformation relationship

Now we express the constitutive relation in terms of the unknown nodal displacements. Note that the constitutive response stems from the peridynamic long-range forces, thus the expression of the constitutive relation is based on the peridynamic elements.

First, the measure of deformation $\boldsymbol{\eta}$ that associated with a peridynamic element $\bar{e}_k$ could be approximately expressed as

$$\bar{\boldsymbol{\eta}}_k\left(\boldsymbol{x}', \boldsymbol{x}\right) = \boldsymbol{u}_j\left(\boldsymbol{x}'\right) - \boldsymbol{u}_i\left(\boldsymbol{x}\right) = \bar{\boldsymbol{B}}_k\left(\boldsymbol{x}', \boldsymbol{x}\right)\bar{\boldsymbol{d}}_k, \tag{14}$$

where

$$\bar{\boldsymbol{B}}_k\left(\boldsymbol{x}', \boldsymbol{x}\right) = \bar{\boldsymbol{H}}\bar{\boldsymbol{N}}\left(\boldsymbol{x}', \boldsymbol{x}\right), \tag{15}$$

is the difference matrix of shape function of $\bar{e}_k$, and

$$\bar{\boldsymbol{H}} = \left[\boldsymbol{I}, -\boldsymbol{I}\right], \tag{16}$$

is the difference operator matrix with $\boldsymbol{I}$ an identity matrix of dimension d.

Then, based on the constitutive equation, i.e. Eq. (1b), the approximate pair force vector $\boldsymbol{f}$ reads

$$\bar{\boldsymbol{f}}_k\left(\boldsymbol{x}', \boldsymbol{x}\right) = \boldsymbol{D}(\boldsymbol{\xi})\bar{\boldsymbol{B}}_k\left(\boldsymbol{x}', \boldsymbol{x}\right)\bar{\boldsymbol{d}}_k, \tag{17}$$

where

$$\boldsymbol{D}(\boldsymbol{\xi}) = c(\boldsymbol{\xi})\mu(\boldsymbol{\xi}, t)\begin{bmatrix} \xi_1^2 & \xi_1\xi_2 & \xi_1\xi_3 \\ \xi_2\xi_1 & \xi_2^2 & \xi_2\xi_3 \\ \xi_3\xi_1 & \xi_3\xi_2 & \xi_3^2 \end{bmatrix}, \tag{18}$$

is the matrix form of the micro-modulus tensor $\boldsymbol{C}(\boldsymbol{\xi})$ for $d = 3$.

3.4. Derive the element stiffness matrix and equations

In this section, we will show how to derive the element stiffness matrix and linear equations about the nodal displacement according to the principle of minimum potential energy.

For any peridynamic element $\bar{e}_k$ that generated from local elements e_i and e_j, the potential energy [28] of $\bar{e}_k$ is

$$\Pi_k(\boldsymbol{u}) = \frac{1}{4}\int_{\bar{e}_k}\int_{\mathcal{H}_{\delta(\boldsymbol{x})}\cap\bar{e}_k}\boldsymbol{f}\left(\boldsymbol{x}', \boldsymbol{x}\right)\cdot\boldsymbol{\eta}\left(\boldsymbol{x}', \boldsymbol{x}\right)\mathrm{d}V_{\boldsymbol{x}'}\mathrm{d}V_{\boldsymbol{x}} - \int_{e_j}\boldsymbol{p}\left(\boldsymbol{x}'\right)\cdot\boldsymbol{u}\left(\boldsymbol{x}'\right)\mathrm{d}V_{\boldsymbol{x}'} - \int_{e_i}\boldsymbol{p}\left(\boldsymbol{x}\right)\cdot\boldsymbol{u}\left(\boldsymbol{x}\right)\mathrm{d}V_{\boldsymbol{x}}, \tag{19}$$

where $\boldsymbol{p}$ is composed of external body forces and the long-range forces associated with the points not belonging to the peridynamic element $\bar{e}_k$, and it is unclear for a certain element [1]. Further, according to the content from Sections 3.2 and 3.3, the potential energy is now a function of the nodal displacements, i.e.,

$$\begin{aligned}\Pi_k(\bar{\boldsymbol{d}}_k) &= \frac{1}{4}\int_{\bar{e}_k}\int_{\mathcal{H}_{\delta(\boldsymbol{x})}\cap\bar{e}_k}\bar{\boldsymbol{f}}_k\left(\boldsymbol{x}', \boldsymbol{x}\right)\cdot\bar{\boldsymbol{\eta}}_k\left(\boldsymbol{x}', \boldsymbol{x}\right)\mathrm{d}V_{\boldsymbol{x}'}\mathrm{d}V_{\boldsymbol{x}} - \int_{e_j}\boldsymbol{p}\left(\boldsymbol{x}'\right)\cdot\boldsymbol{u}_j\left(\boldsymbol{x}'\right)\mathrm{d}V_{\boldsymbol{x}'} - \int_{e_i}\boldsymbol{p}\left(\boldsymbol{x}\right)\cdot\boldsymbol{u}_i\left(\boldsymbol{x}\right)\mathrm{d}V_{\boldsymbol{x}} \\ &= \frac{1}{4}\bar{\boldsymbol{d}}_k^T\bar{\boldsymbol{K}}_k\bar{\boldsymbol{d}}_k - \bar{\boldsymbol{d}}_k^T\bar{\boldsymbol{P}}_k,\end{aligned} \tag{20}$$

[1] Although it is unclear for a certain element, it does not matter as we need the total external force vector after assembling the whole structure.

where

$$\bar{\boldsymbol{K}}_k = \int_{\bar{e}_k} \int_{\mathcal{H}_{\delta(\boldsymbol{x})} \cap \bar{e}_k} \bar{\boldsymbol{B}}_k^T \left(\boldsymbol{x}', \boldsymbol{x}\right) \boldsymbol{D}(\boldsymbol{\xi}) \bar{\boldsymbol{B}}_k \left(\boldsymbol{x}', \boldsymbol{x}\right) \mathrm{d}V_{\boldsymbol{x}'} \mathrm{d}V_{\boldsymbol{x}}, \tag{21}$$

$$\bar{\boldsymbol{P}}_k = \begin{bmatrix} \int_{e_j} \boldsymbol{N}_j^T \left(\boldsymbol{x}'\right) \boldsymbol{p}\left(\boldsymbol{x}'\right) \mathrm{d}V_{\boldsymbol{x}'} \\ \int_{e_i} \boldsymbol{N}_i^T \left(\boldsymbol{x}\right) \boldsymbol{p}\left(\boldsymbol{x}\right) \mathrm{d}V_{\boldsymbol{x}} \end{bmatrix}. \tag{22}$$

Then, taking the first variation, we have

$$\frac{1}{2} \bar{\boldsymbol{K}}_k \bar{\boldsymbol{d}}_k = \bar{\boldsymbol{P}}_k. \tag{23}$$

3.5. Assemble the element equations

With the element stiffness matrix at hand, we now can assemble the global stiffness matrix, the global force vector, and the global linear equations.

For convenience, we introduce the transform matrix of the degree of freedom for the nodes of $\bar{e}_k$, denoted as $\bar{\boldsymbol{G}}_k$, which satisfies

$$\bar{\boldsymbol{d}}_k = \bar{\boldsymbol{G}}_k \boldsymbol{d}, \tag{24}$$

where $\boldsymbol{d}$ is the total nodal displacement vector, then we have the global linear equations

$$\frac{1}{2} \bar{\boldsymbol{K}} \boldsymbol{d} = \bar{\boldsymbol{P}}, \tag{25}$$

where

$$\bar{\boldsymbol{K}} = \sum_{k=1}^{\bar{m}} \bar{\boldsymbol{G}}_k^T \bar{\boldsymbol{K}}_k \bar{\boldsymbol{G}}_k, \tag{26}$$

$$\bar{\boldsymbol{P}} = \sum_{k=1}^{\bar{m}} \bar{\boldsymbol{G}}_k^T \bar{\boldsymbol{P}}_k, \tag{27}$$

are the global stiffness matrix and the global force vector, respectively.

Besides, one should note that $\bar{\boldsymbol{P}}_k$ is unclear for a certain peridynamic element, so it is infeasible to calculate $\bar{\boldsymbol{P}}$ using Eq. (27). But for the whole structure, $\bar{\boldsymbol{P}}$ represent the external force that applied on Ω, thus

$$\bar{\boldsymbol{P}} = \boldsymbol{F} = \sum_{i=1}^{m} \boldsymbol{G}_i^T \boldsymbol{F}_i, \tag{28}$$

where

$$\boldsymbol{F}_i = \int_{e_i} \boldsymbol{N}_i^T(\boldsymbol{x}) \boldsymbol{b}(\boldsymbol{x}) \mathrm{d}V_{\boldsymbol{x}}, \tag{29}$$

$\boldsymbol{G}_i$ is the transform matrix of the degree of freedom for the nodes of e_i and satisfies

$$\boldsymbol{d}_i = \boldsymbol{G}_i \boldsymbol{d}. \tag{30}$$

Remark 1. *Note that PeriFEM is also suitable for dual-horizon peridynamics [29].*

4. Numerical algorithm

4.1. Algorithm of PeriFEM

In this subsection, we introduce the algorithm of PeriFEM. Considering that the failure progress of structures involves material nonlinearity, the boundary conditions are applied progressively in N incremental steps. More details of the algorithm are shown in Fig. 2, the flowchart of PeriFEM.

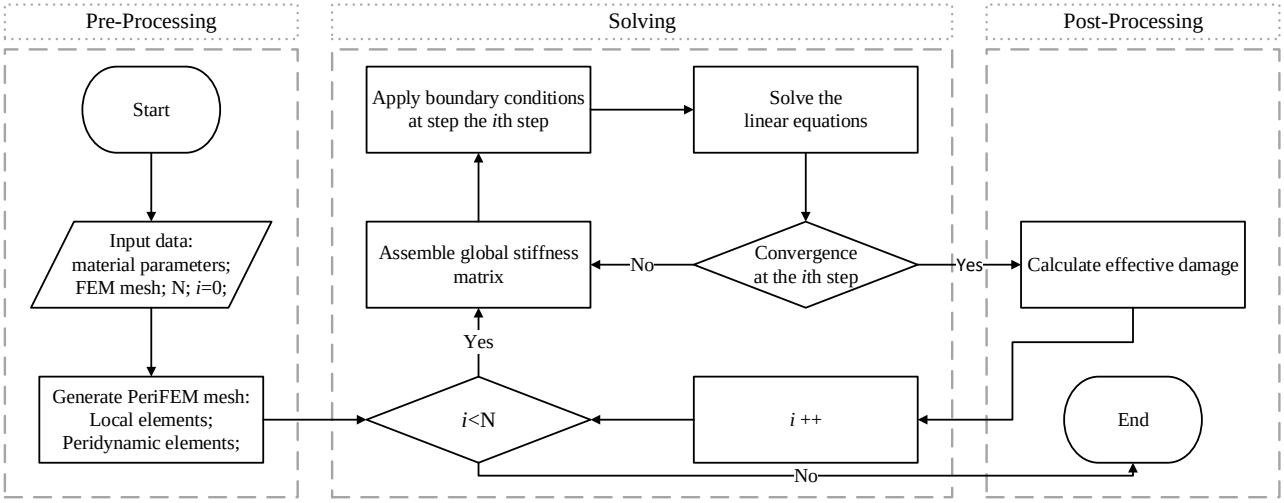

Figure 2: Algorithm of PeriFEM.

As shown in Fig. 2, the simulation process could be divided into three parts: pre-processing, solving, and post-processing. In the pre-processing stage, some necessary data, such as the material parameters, the FEM mesh, and the number of incremental steps N, should be input, and the PeriFEM mesh needs to be generated based on the FEM mesh. In the solving stage, the simulation is executed progressively at each incremental step. Each incremental step may contain several iterations, i.e., Eq. (25) may be solved several times until the convergence criterion is satisfied (the convergence criterion will be addressed in the next subsection). Once the results converge, the effective damage is calculated to reveal the cracks. Then, the next incremental step is executed. When all incremental steps are completed, the simulation ends.

4.2. Convergence criteria

This subsection is devoted to the convergence criterion at a certain incremental step. We will introduce two criteria: one is a bond-based criterion, the other is an equilibrium-based criterion.

Bond-based criterion. During the numerical implementation, the definition of bonds is associated with the quadrature points in peridynamic elements, as shown in Fig. 3. For more details about the bond, readers can refer to [22]. The convergence criterion is based on the information of broken bonds. In precise, for a certain incremental step, if there is no new-broken bond after Eq. (25) is solved, we claim that the results converge at this step.

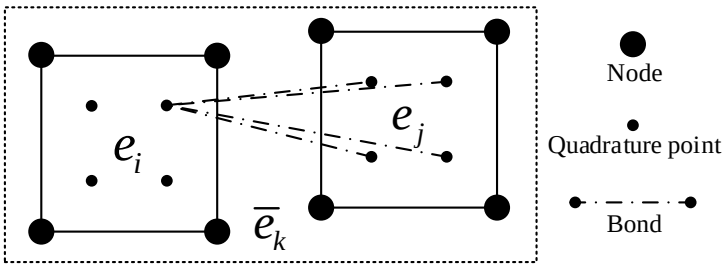

Figure 3: Schematic of bonds in a peridynamic element.

Equilibrium-based criterion. The equilibrium-based criterion is the default criterion in ABAQUS, which is based on the equilibrium between the external forces and internal forces [30]. For the jth iteration in the ith incremental step, we can obtain the global nodal displacement vector, denoted by $\boldsymbol{d}^{i,j}$, by solving Eq. (25), then, the status μ of each bond could be updated according to $\boldsymbol{d}^{i,j}$. Based on $\boldsymbol{d}^{i,j}$ and μ, we can calculate the nodal forces (i.e., internal forces) vector, denoted by $\boldsymbol{Q}^{i,j}$, then define the residual forces vector for this iteration as

$$\boldsymbol{R}^{i,j} = \boldsymbol{F}^{i} - \boldsymbol{Q}^{i,j}, \tag{31}$$

where $\boldsymbol{F}^{i}$ is the external force vector at this incremental step. We claim that the results converge at this step if $\left\|\boldsymbol{R}^{i,j}\right\|$ is smaller than a given tolerance.

5. Implementation of PeriFEM in FEM software

5.1. Implementation of PeriFEM in ABAQUS

In ABAQUS, it is not convenient to extract the broken-bond information for users, thus the equilibrium-based convergence criterion (i.e., the default convergence criterion in ABAQUS) is used. Namely, the incremental steps and the iterations in each step are completely controlled by ABAQUS.

Fig. 4 shows the relation between the subroutines and ABAQUS. At the beginning of the incremental step, the calculation model data is read in from the input file (.inp), including the material data (PROPS), such as the critical stretch and the micro-modulus, and the geometry data (COORDS), such as node coordinates, element nodes, and element number, as well as user-defined element information such as peridynamic element nodes and element number. For each iteration, the element stiffness matrices (AMATRX), the right-hand-side vectors (RHS), and the state variables (SVARS), which are used to store the broken-bond information during internal computation, etc. are calculated and updated in UEL. At the end of this incremental step, the updated variable information is transmitted to the ABAQUS main program by the UEL subroutine interface. Then, in the UMAT subroutine, the broken-bond and damaged information are stored in the state variable (STATEV) through the transfer of global variables. Finally, the results, including displacement fields and damage fields can be displayed in the contours of ABAQUS results.

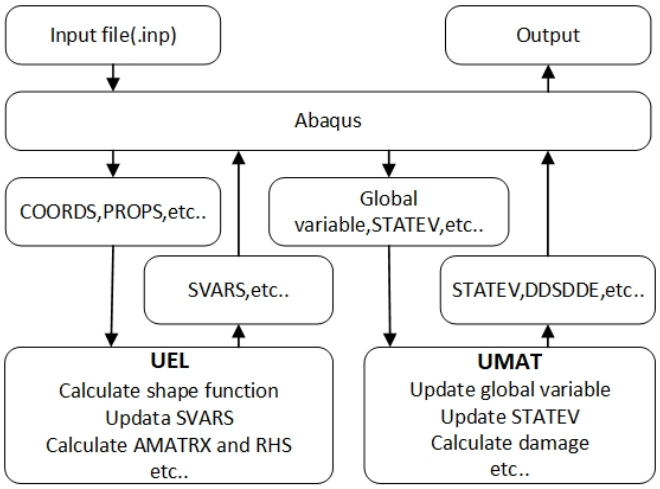

Figure 4: ABAQUS implementation details of PeriFEM using UEL and UMAT.

In addition, it should be pointed out that although the stiffness matrix in ABAQUS is obtained entirely based on the peridynamic elements (a user-defined element type), we also need a set of local elements (the native ABAQUS elements or known as the background elements) for the following two reasons: (1) The peridynamic elements is generated from the local elements, as detailed in Section 3.1, and (2) The post-processor of ABAQUS does not support the user-defined elements. Therefore, to enable the visualization of the simulated results in ABAQUS, the native ABAQUS elements are essential. The process of the visualization could be summarized as: the broken-bond information (SVARS) is obtained in UEL firstly, then SVARS is passed into UMAT via the global variable (a user-defined variable), based on which the damage information (STATEV) could be obtained according to Eq. (7), and finally, the damage could be visualized through the local elements.

5.2. Implementation of PeriFEM in ANSYS

In ANSYS, APDL allows to extract the broken-bond information from UserElem conveniently, thus the bond-based convergence criterion is used. Namely, the incremental steps and iterations in each step are completely controlled by APDL (i.e., controlled by users).

Fig. 5 shows the relation between the subroutines and ANSYS. At the beginning of the incremental step, the calculation model data is read in from the input file (.cdb), including the material data, such as the critical stretch and the micro-modulus, and the geometry data (ELEM, node), such as node coordinates (node), element nodes and element number (ELEM), as well as the node and element number in the user-defined peridynamic element based on UPFs. For each iteration, the element stiffness matrices (estiff) and element broken-bond information (stored in Rsltvar) based on peridynamic elements are computed and updated in UserElem. At the end of the incremental step, the broken-bond information is transmitted to the ANSYS main program. Finally, the damage is evaluated based on the broken-bond information in the main program, and then the damage is displayed directly through the GUI interface.

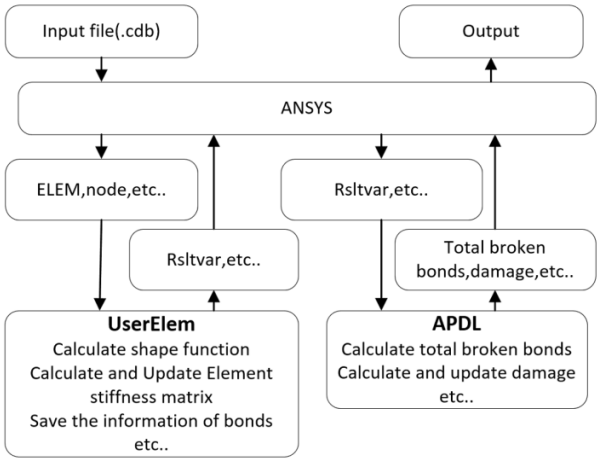

Figure 5: ANSYS implementation details of PeriFEM using APDL and UserElem.

In addition, we also need both peridynamic elements and local elements in ANSYS stated in the previous subsection. And the only difference is how damage information is obtained. The process of the visualization in ANSYS could be summarized as: the broken-bond information (Rsltvar) is obtained in UserElem subroutine firstly, then RsltVar is extracted from UserElem by APDL, based on which the damage information for each local element could be calculated according to Eq .(7), and finally, the damage contour could be displayed in the *postprocess* module of ANSYS via the local elements .

Remark 2. *PeriFEM allows both continuous and discrete local elements [22] in essence, but as FEM software, only continuous local element is available in ABAQUS and ANSYS, thus only the continuous local element is used in the present paper.*

6. Numerical examples

6.1. 2D test for the verification and comparison of ANSYS and ABAQUS

On the one hand, the first purpose of this section is to verify the codes of PeriFEM in ANSYS and ABAQUS. On the other hand, as different convergence criteria were adopted in ANSYS and ABAQUS, the convergence performance, the computational cost, and the predicted crack patterns need to be compared between ANSYS and ABAQUS. To this end, 2D benchmark examples are carried out with both ANSYS and ABAQUS in this section.

6.1.1. Single-edge-notched plate under a tension test

We first consider a tension test for a single-edge-notched plate. The geometry and boundary conditions are demonstrated in Fig. 6. The Young's modulus is $E = 200$ GPa, the Poisson's ratio is $\nu = 1/3$, the critical stretch is $s_{crit} = 0.02$. The plate is discretized with quadrilateral local elements and the mesh size is $h = 5$ mm. The horizon is chosen as $\delta = 3h$ and 9860 peridynamic elements are generated. The boundary conditions are divided into 100 incremental steps.

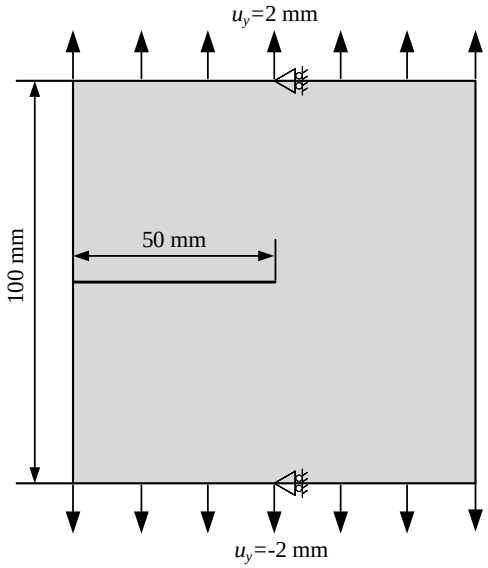

Figure 6: Geometry and boundary conditions of a single-edge-notched plate.

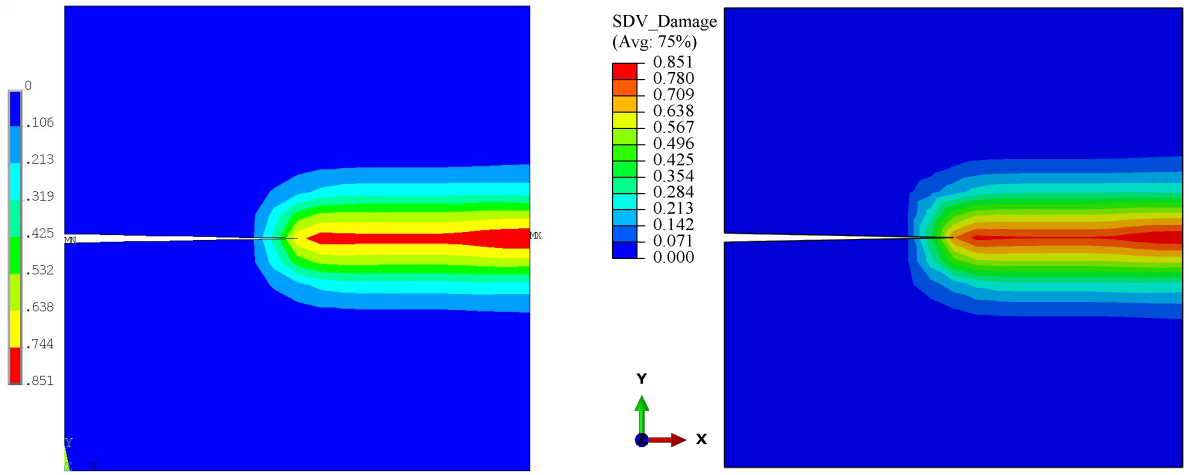

(a) (b)

Figure 7: Contours of the effective damage for single-edge-notched plate computed by (a): ANSYS and (b): ABAQUS.

It is known that the crack will initiate from the notch tip and propagate horizontally to the right for this test. As shown in Fig. 7, the effective damage contours, which reveal the crack, predicted by ANSYS and ABAQUS are correct. It verifies that the code of PeriFEM integrated into ANSYS and ABAQUS are correct. Moreover, Fig. 8(a) shows the iteration numbers in each incremental step of both ANSYS and ABAQUS. It can be seen that the iteration number of them are almost coincided with each other for this test, although different convergence criteria are adopted. Fig. 8(b) displays the total computational costs of both ANSYS and ABAQUS. As the total iteration numbers of ANSYS and ABAQUS are similar, it can be concluded that the computational cost of ABAQUS in one iteration step is less than ANSYS.

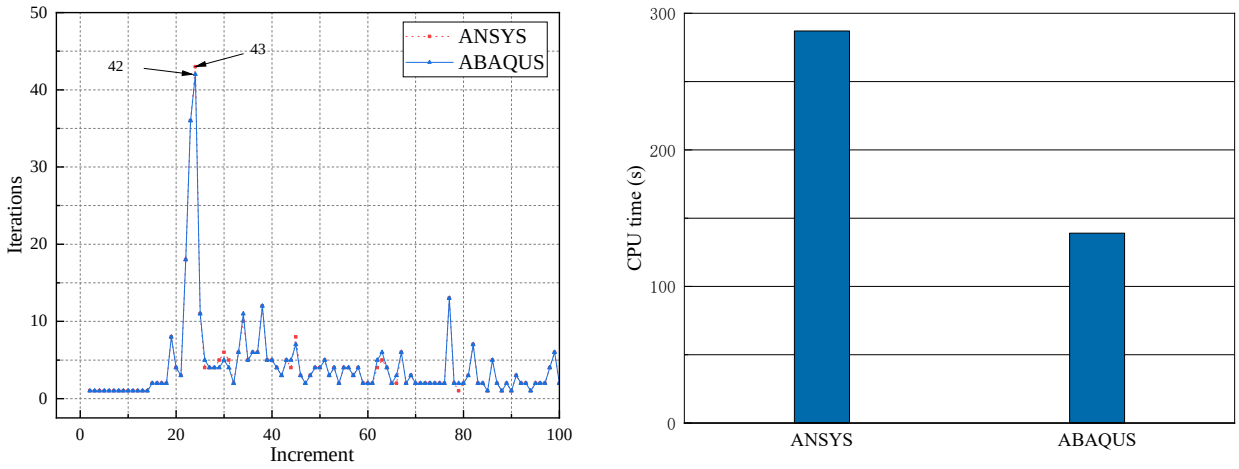

(a) (b)

Figure 8: Comparison of iteration number in each incremental step and CPU time between ANSYS and ABAQUS.

6.1.2. L-shaped panel test

We now consider an L-shaped panel. The geometry and boundary conditions are depicted in Fig. 9. The Young's modulus is $E = 25.85$ GPa, the Poisson's ratio is $\nu = 1/3$, the critical stretch is $s_{crit} = 0.0006$. The panel is discretized with quadrilateral local elements and the mesh size is $h \approx 3.6$ mm. The horizon is chosen as $\delta = 3h$ and 909262 peridynamic elements are generated. The boundary conditions are divided into 140 incremental steps.

Figs. 10(a) and (b) display the predicted effective damage zones by ANSYS and ABAQUS, respectively, and Fig. 10(c) compares the predicted crack path with the experimental failure zone reported in [31]. Both simulated results by ANSYS and ABAQUS are in good agreement with experiment data, which further verify the developed code. Moreover, Fig. 11 shows the iteration numbers in each incremental step by ANSYS and ABAQUS, the similarity of such two curves indicates that the simulated results by ANSYS and ABAQUS are in line with each other.

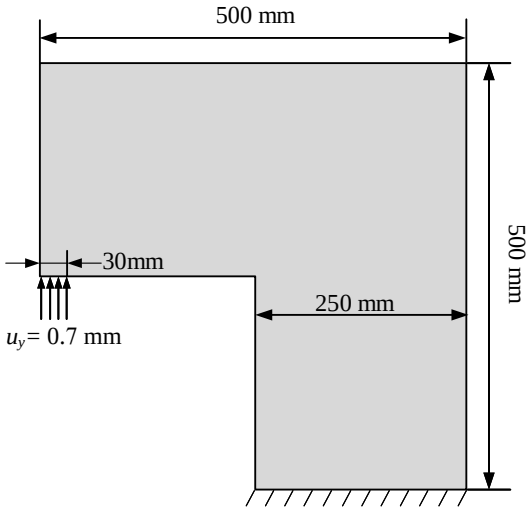

Figure 9: Geometry and boundary condition of an L-shaped panel.

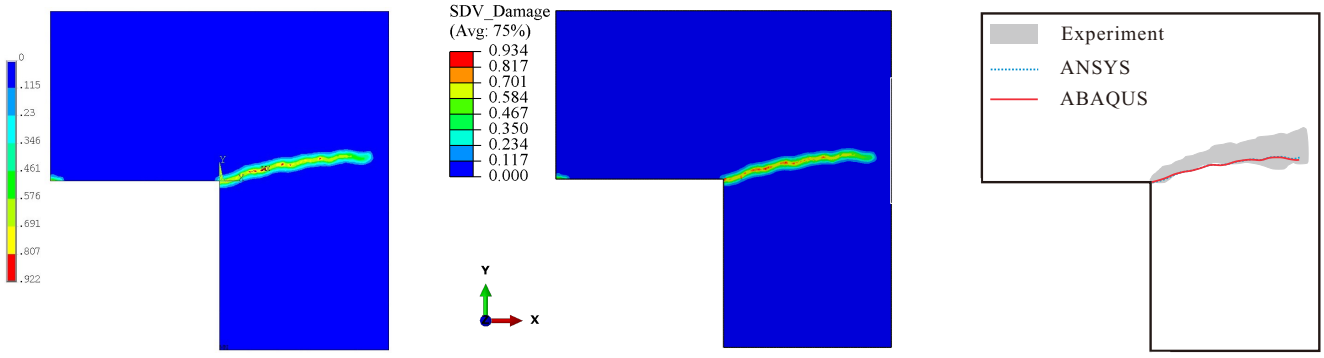

(a) (b) (c)

Figure 10: Contours of the effective damage for an L-shaped panel computed by (a): ANSYS, (b): ABAQUS and (c): a comparison with experimental results.

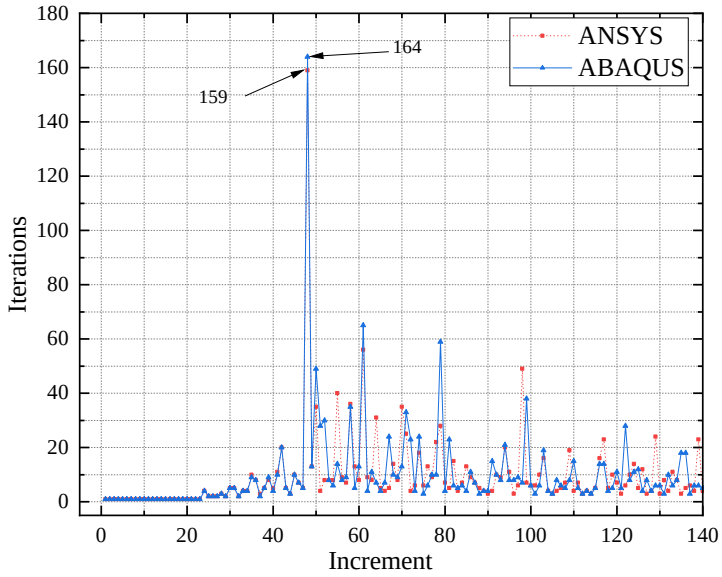

Figure 11: Comparison of iteration numbers in each incremental step between ANSYS and ABAQUS..

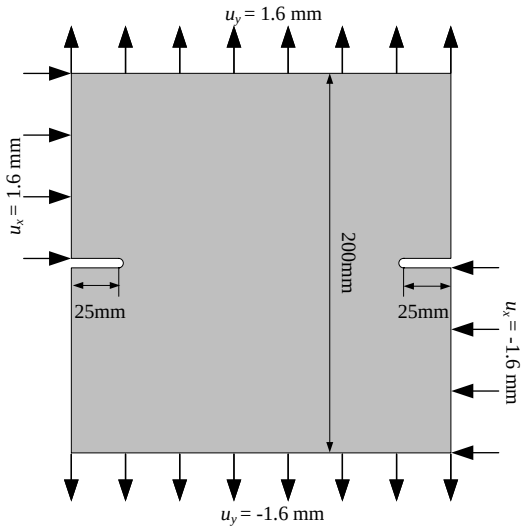

Figure 12: Geometry and boundary condition of a double-edge-notched plate.

6.1.3. Double-edge-notehed plate under tension and shear test

For this test, we investigate the mixed mode fracture of a double-edge-notched plate. The geometry and boundary conditions are shown in Fig. 12. The Young's modulus is $E = 30$ GPa, the Poisson's ratio is $\nu = 1/3$, the critical stretch is $s_{crit} = 0.02$. The plate is discretized with quadrilateral local elements and the mesh size is $h \approx 1.25$ mm. The horizon is set as $\delta = 3h$ and 1019120 peridynamic elements are generated. The boundary conditions are divided into 80 incremental steps.

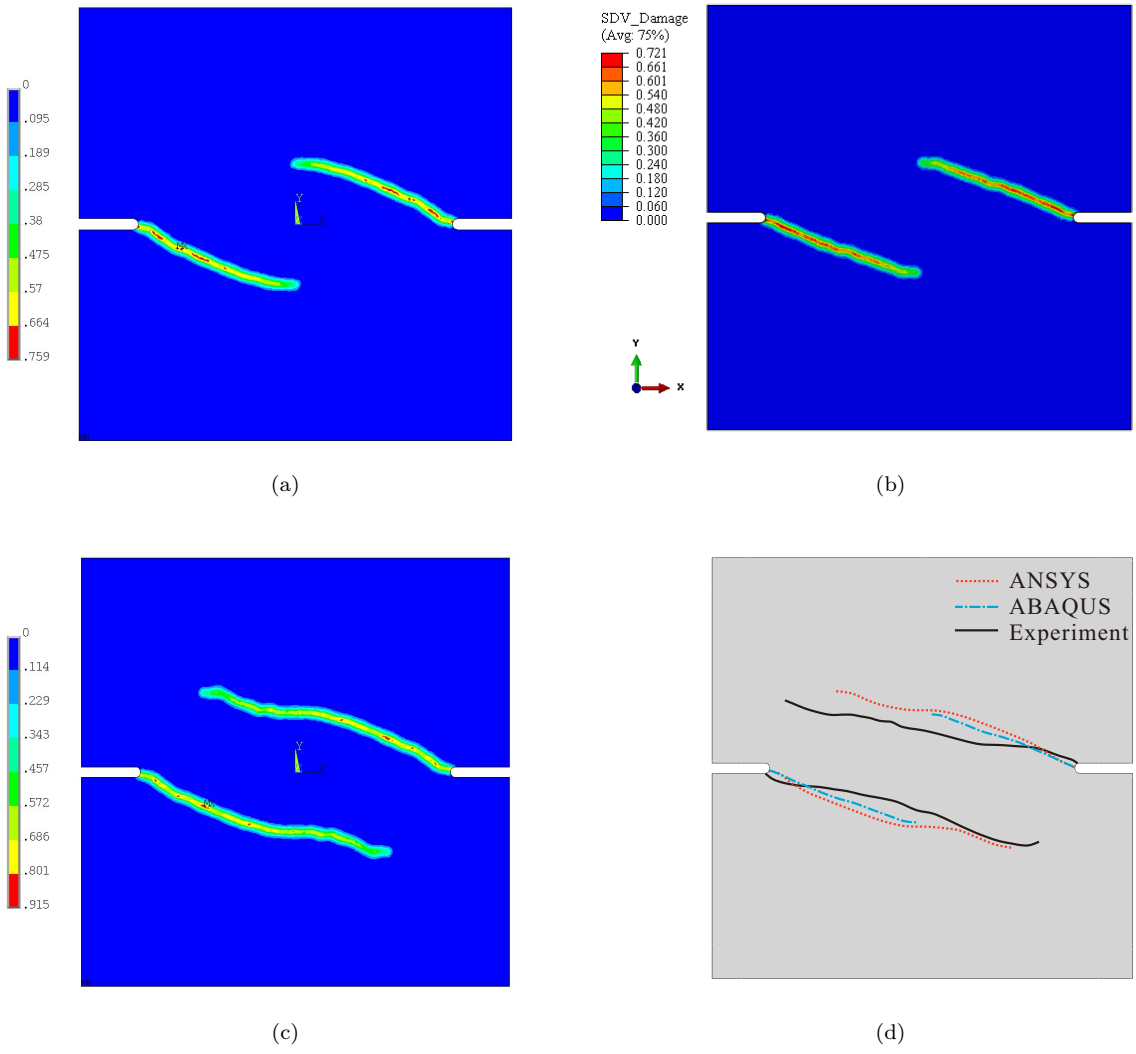

Figure 13: Contours of the effective damage for double-edged plate with (a): ANSYS at 20th incremental step, (b): ABAQUS at 20th incremental step, (c): ANSYS at 80th incremental step and (d): a comparison with experimental results.

The predicted effective damage contours and its comparison with the experimental results [32] are shown in Fig. 13. It can be seen that the predicted crack paths are in well with the experimental results. On the other hand, one may note that the simulated result by ABAQUS are only for the 20th incremental step, but not for

the 80th incremental step. This is because from the 21st increment, ABAQUS encounters a convergence issue, as shown in Fig. 14. Figs. 14(a) and (b) display the number of broken bonds and the largest residual force during the iteration, respectively. Although the number of broken bonds no longer increases, the largest residual force still does not satisfy the convergence condition, and fall into a regular oscillation, which means that the iteration will never converge.

Remark 3. *The above non-convergence phenomenon is not a problem of the code but may steam from the constitutive model and the specimen. And it has been reported in [33] that the discontinuity of the constitutive model will result in convergence issues.*

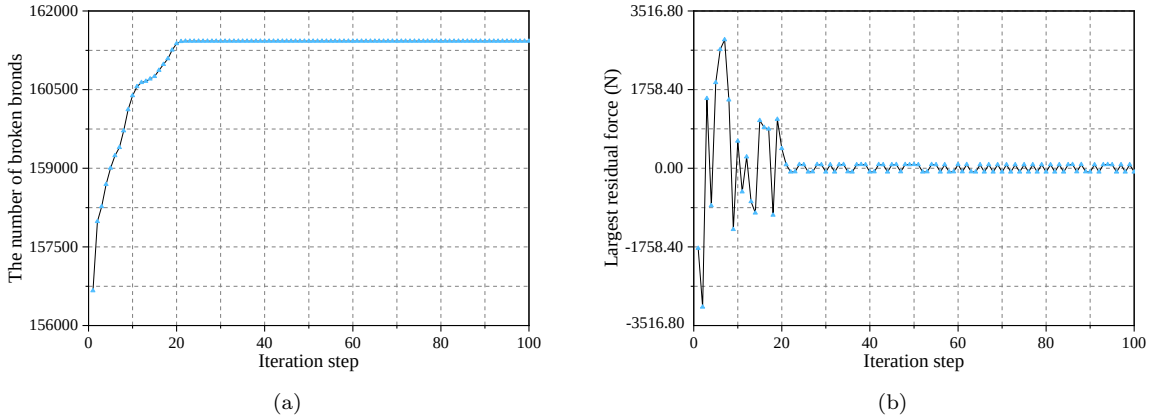

Figure 14: The iteration information of ABAQUS at the 21st incremental step. (a): the number of broken bonds, (b): the largest residual force.

6.2. 3D test

Now we investigate the 3D examples with ANSYS and ABAQUS to verify the ability of the proposed method in dealing with complex problems. In all tests, hexahedral local element are used.

6.2.1. Three point bending test on slanted notched beam

This example shows a three point bending test of a beam with a slanted notch. That is, a vertical notch with an inclination of $\theta = 45^\circ$ with respect to the longitudinal mid-plane of the beam, is set. We consider the same geometry and boundary conditions as reported in [34], which are presented in Fig. 15.

The Young's modulus is $E = 2.8$ GPa, the Poisson's ratio is $\nu = 1/4$, the critical stretch is $s_{crit} = 0.00235$. The beam is discretized with hexahedral local elements and the mesh size is $h \approx 2.0$ mm. The horizon is set as $\delta = 3h$, and 1618634 peridynamic elements are generated. The prescribed displacement is equally divided into 100 incremental steps.

ABAQUS is used in this test. The predicted effective damage contours are shown in Fig. 16. It can be seen that the crack face initially propagates along the direction of the slanted notch, and then it twists gradually in

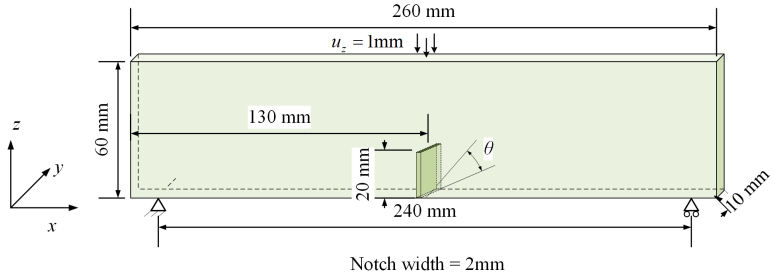

Figure 15: Geometry and boundary condition of slanted notched beam.

space with the increasing prescribed displacement due to the angle between the notch direction and the applied load direction (along the mid-plane). And finally it aligns with the mid-plane. It can be concluded that the torsion of the crack surface has been captured in the simulation, although the torsion is not very obvious, which is due to the limitation of computational resources that the mesh is not fine enough. It also shows that the proposed technique can be successfully applied to 3D problems.

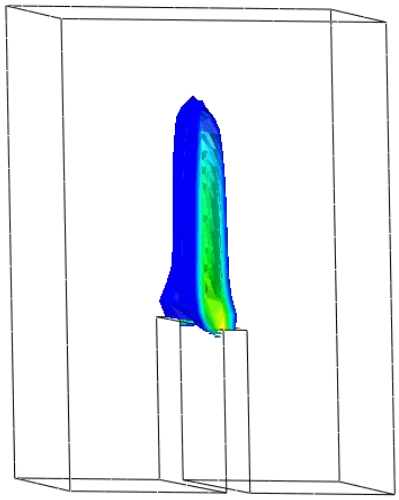

Figure 16: Crack pattern and damage profile.

For better observability, the prospective views of the damage profile at various heights above the notch are shown in Fig. 17. We used two reference (white) lines, one marking the main damage zone and the other marking the direction of slanted notch, to show the rotation angle of the main damage zone. The difference of the revolving angles at different heights reveals the rotation of the damage field. The damage starts from the slanted notch, and then it twists spatially and develops along the vertical direction. At first, the damage field's revolving angle increases rapidly, and then it increases slowly. Finally, the top view of the damage profile is nearly along the mid-plane of the geometric model.

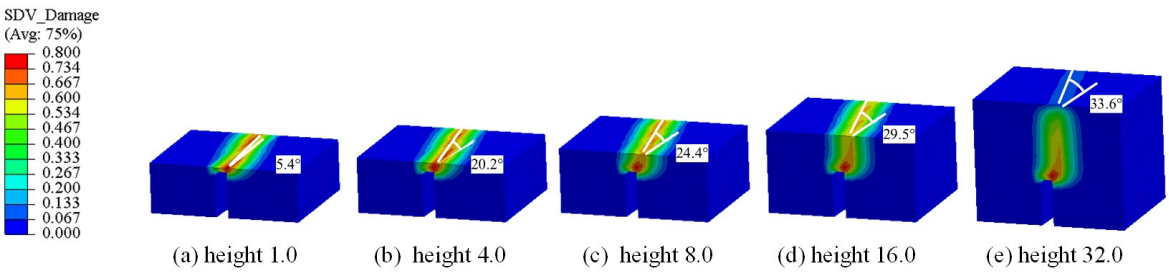

Figure 17: Predicted damage profile at different heights above the notch.

6.2.2. Prismatic skew notched beam under torsion

Finally, a prismatic skew edge notched concrete beam under torsion is simulated by ANSYS. This example was also tested by Brokenshire [35] and reported in detail in [36]. The geometry and boundary conditions of the beam are shown in Fig. 18.

The Young's modulus is $E = 35$ GPa, the Poisson's ratio is $\nu = 1/4$, the critical stretch is $s_{crit} = 0.0006316$. The beam is discretized with hexahedral local elements and the mesh size is $h \approx 5$ mm. The horizon is set as $\delta = 3h$ and 3886626 peridynamic elements are generated. The prescribed displacement is equally divided into 50 incremental steps.

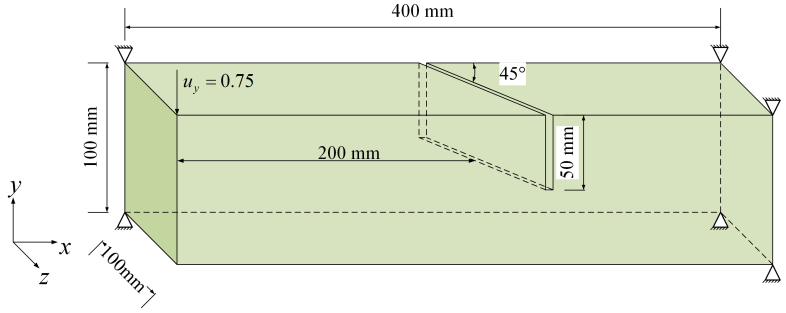

Figure 18: Geometry and boundary condition of prismatic skew notched beam.

Fig. 19 shows the displacement contour and three different views of the damage iso-surface at the last incremental step. Fig. 19(a) displays the displacement contour of the beam. The discontinuities of displacement can be clearly observed as expected, which indicates crack nucleation. Figs. 19(b), (c) and (d) show the top view, slanted view and side view of damage iso-surface, respectively. The skew-symmetrical crack surface with a complex twisting pattern can be clearly observed from such three different views.

Fig. 20 shows three top views of damage iso-surface obtained from three different methods. Fig. 20(a) is simulated by ANSYS using PeriFEM, Fig. 20(b) is obtained from the experiment on PMMA [37], and Fig. 20(c) is simulated by ABAQUS using the phase-field method [34]. The crack surface in Fig. 20(a) is similar to those in Fig. 20(b) and (c). Meanwhile, the above results are consistent with those obtained from the isotropic damage model in the context of stabilized mixed finite elements [38], which could demonstrate the feasibility

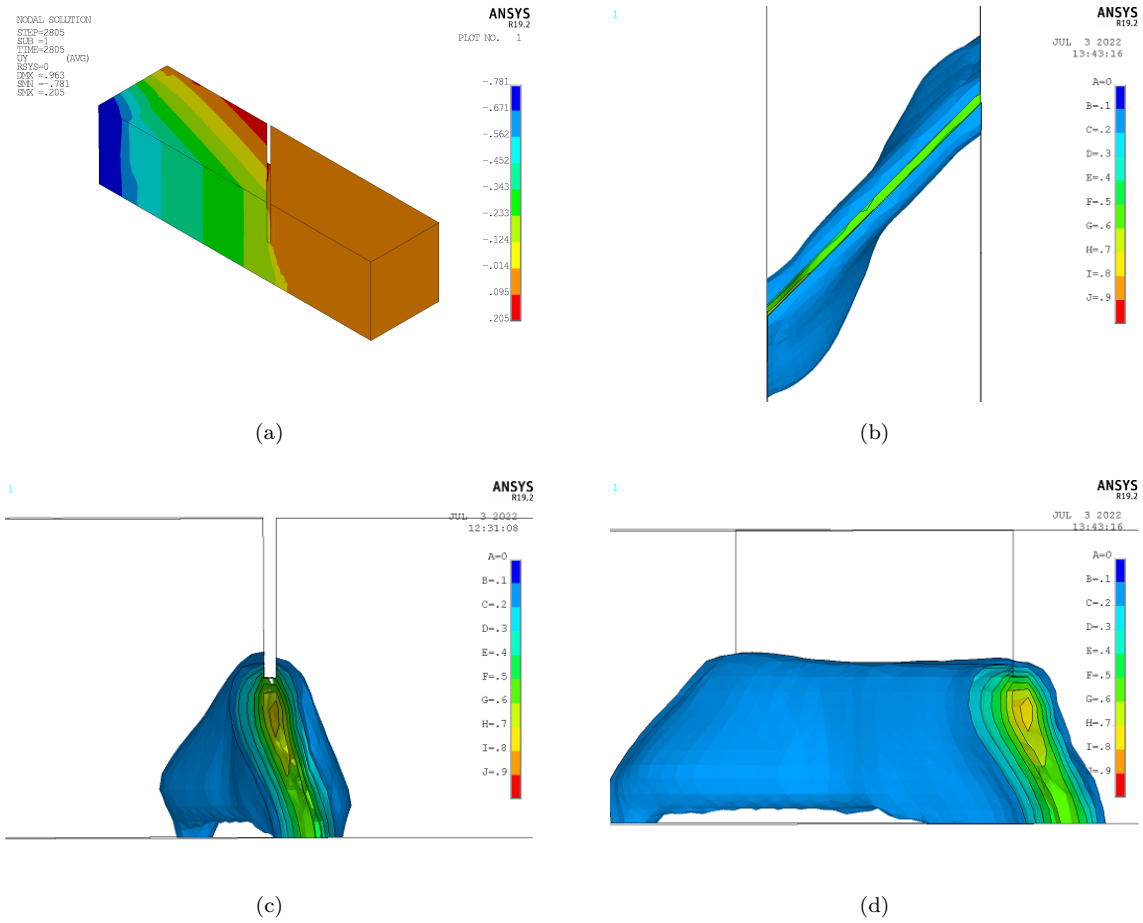

Figure 19: Displacement contour and damage iso-surface of concrete beam at the last incremental step: (a) displacement contour; (b) top view of damage iso-surface; (c) slanted view of damage iso-surface; (d) side view of damage iso-surface.

of using PeriFEM in ANSYS to simulate 3D problems. Note that though the maximum vertical displacement in ANSYS is 0.75mm, which is half of 1.5mm in experimental test and ABAQUS simulation, according to the load-displacement curve in [34], the beam completely fractures when vertical displacement is 0.75mm.

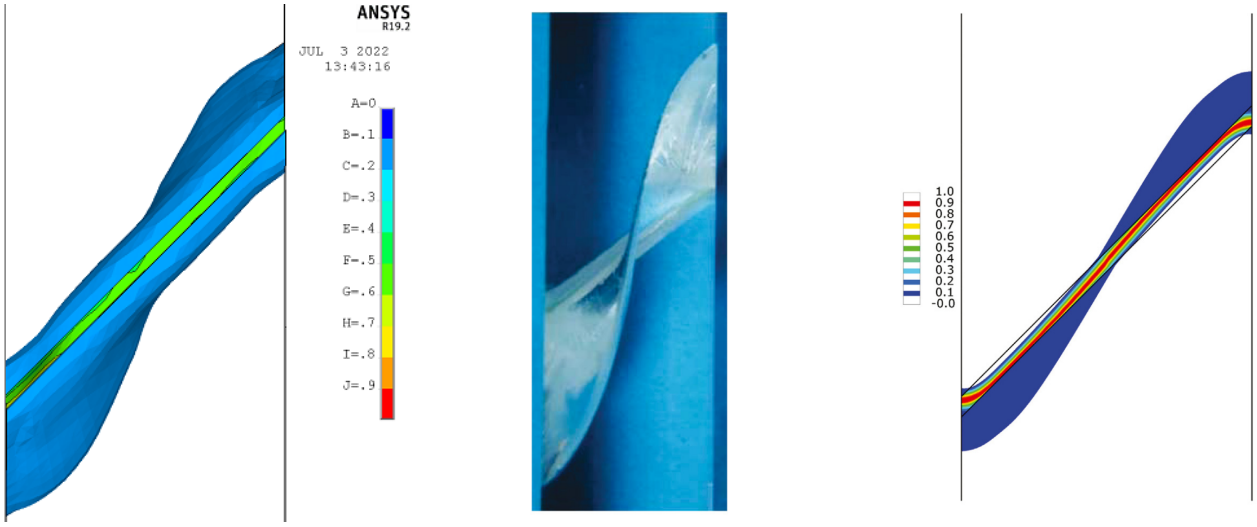

(a) (b) (c)

Figure 20: Top view of damage surface obtained from different methods: (a) from ANSYS using PeriFEM; (b) from PMMA test [37]; (c) from ABAQUS using the phase-field method [34].

7. Conclusions

This paper present the implementation details of the preidynamics-based finite element method (PeriFEM) in ANSYS and ABAQUS. Benefited by the consistency of PeriFEM and classical finite element method calculation framework, it is convenient for us to realize the failure simulation using peridynamics in ANSYS and ABAQUS. Further more, in light of the similarity of the implementation of PeriFEM in ANSYS and ABAQUS, it is easy for users to extend PeriFEM in other FEM software. 2D and 3D numerical examples verifies the proposed method. Therefore, the current work facilitates the application of peridynamics in engineering practice.

Acknowledgments

The authors gratefully acknowledge the financial support received from the National Natural Science Foundation of China (11872016), National Key Laboratory of Shock Wave and Detonation Physics (JCKYS2021212003).

Appendix A. The calculation of $\tilde{c}(\theta, \varphi)$ for anisotropic materials

In 2013, Azdoud et al. [39] derived the expression of $c(\boldsymbol{\xi})$ based on the real spherical harmonic expansion technique, where $\tilde{c}(\theta, \varphi)$ in Eq. (4) was defined as

$$\tilde{c}(\theta, \varphi) = a_{00} + \sum_{k=1}^{+\infty} \left[\sum_{m=0}^{k} P_k^m(\cos(\theta)) \left(a_{km} \cos(m\varphi) + b_{km} \sin(m\varphi) \right) \right], \tag{A.1}$$

where θ and φ supplemented with $\|\boldsymbol{\xi}\|$ compose the spherical coordinates of bond $\boldsymbol{\xi}$, as shown in Fig. A.21. a_{00}, a_{km} and b_{km} are real parameters, P_k^m are Legendre functions. And they have shown that for *orthotropic model*,

$$\begin{aligned} \tilde{c}(\theta, \varphi) =& a_{00} + a_{20} P_2^0(\cos(\theta)) + a_{22} \cos(2\phi) P_2^2(\cos(\theta)) + \\ & a_{40} P_4^0(\cos(\theta)) + a_{42} \cos(2\phi) P_4^2(\cos(\theta)) + a_{44} \cos(4\phi) P_4^4(\cos(\theta)), \end{aligned} \tag{A.2}$$

for *transverse isotropic model* (supposing $\boldsymbol{e}_3$ is the reference direction of the axisymmetry material),

$$\tilde{c}(\theta, \varphi) = \tilde{c}(\theta) = a_0 + a_2 P_2^0(\cos\theta) + a_4 P_4^0(\cos\theta). \tag{A.3}$$

In addition, they have also given the expression of real parameters in Eqs. (A.2) and (A.3) for $\hat{c}(\|\boldsymbol{\xi}\|) = 1$. But they have not told us how to calculate these real parameters, thus it is difficult to determine the real parameters for $\hat{c}(\|\boldsymbol{\xi}\|) \neq 1$.

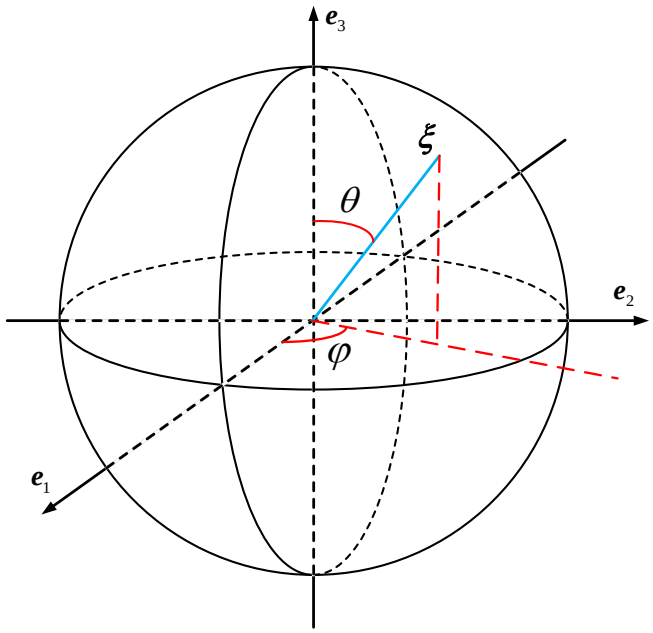

Figure A.21: The spherical coordinates of bond $\boldsymbol{\xi}$.

In fact, the parameters in Eqs. (A.2) and (A.3) could be determined according to the deformation energy equivalence, and the key point is to define an equivalent stiffness tensor. Based on the assumption of uniform

strain fields, Lubineau et al. derived an effective stiffness tensor as [25]

$$\boldsymbol{D} = \int_{H_\delta(\boldsymbol{x})} \frac{c(\boldsymbol{\xi})}{2} \boldsymbol{\xi} \otimes \boldsymbol{\xi} \otimes \boldsymbol{\xi} \otimes \boldsymbol{\xi} \mathrm{d}V_{\boldsymbol{x}'}, \tag{A.4}$$

Denote the classical stiffness tensor as $\boldsymbol{E}$, set

$$\boldsymbol{D} = \boldsymbol{E}, \tag{A.5}$$

then we can determine the parameters.

Appendix A.1. The orthotropic model

For classical orthotropic model, there are 9 independent variables in $\boldsymbol{E}$, which are

$$E_{1111}, E_{2222}, E_{3333}, E_{1122}, E_{1133}, E_{2233}, E_{1212}, E_{1313}, E_{2323}. \tag{A.6}$$

For peridynamic orthotropic model, there are only 6 independent variables in $\boldsymbol{D}$ due to the centrosymmetry of the long range force, which are

$$D_{1111}, D_{2222}, D_{3333}, D_{1122} = D_{1212}, D_{1133} = D_{1313}, D_{2233} = D_{2323}. \tag{A.7}$$

Therefore, Eq. (A.5) means

$$D_{1111} = E_{1111}, D_{2222} = E_{2222}, D_{3333} = E_{3333}, D_{1122} = E_{1122}, D_{1133} = E_{1133}, D_{2233} = E_{2233}. \tag{A.8}$$

Substituting Eq. (A.2) into Eq. (A.4), we have

$$\boldsymbol{D} = a_{00}\boldsymbol{D}^{00} + a_{20}\boldsymbol{D}^{20} + a_{22}\boldsymbol{D}^{22} + a_{40}\boldsymbol{D}^{40} + a_{42}\boldsymbol{D}^{42} + a_{44}\boldsymbol{D}^{44}, \tag{A.9}$$

where

$$\boldsymbol{D}^{ij} = \int_{H_\delta(\boldsymbol{x})} \frac{c^1(\|\boldsymbol{\xi}\|) cos(j\varphi) P_i^j(cos(\theta))}{2} \boldsymbol{\xi} \otimes \boldsymbol{\xi} \otimes \boldsymbol{\xi} \otimes \boldsymbol{\xi} \mathrm{d}V_{\boldsymbol{x}'}, \quad i, j = 0, 2, 4 \text{ and } j \leq i. \tag{A.10}$$

Then, Eq. (A.8) means

$$\begin{bmatrix} D_{1111}^{00} & D_{1111}^{20} & D_{1111}^{22} & D_{1111}^{40} & D_{1111}^{42} & D_{1111}^{44} \\ D_{2222}^{00} & D_{2222}^{20} & D_{2222}^{22} & D_{2222}^{40} & D_{2222}^{42} & D_{2222}^{44} \\ D_{3333}^{00} & D_{3333}^{20} & D_{3333}^{22} & D_{3333}^{40} & D_{3333}^{42} & D_{3333}^{44} \\ D_{1122}^{00} & D_{1122}^{20} & D_{1122}^{22} & D_{1122}^{40} & D_{1122}^{42} & D_{1122}^{44} \\ D_{1133}^{00} & D_{1133}^{20} & D_{1133}^{22} & D_{1133}^{40} & D_{1133}^{42} & D_{1133}^{44} \\ D_{2233}^{00} & D_{2233}^{20} & D_{2233}^{22} & D_{2233}^{40} & D_{2233}^{42} & D_{2233}^{44} \end{bmatrix} \begin{bmatrix} a_{00} \\ a_{20} \\ a_{22} \\ a_{40} \\ a_{42} \\ a_{44} \end{bmatrix} = \begin{bmatrix} E_{1111} \\ E_{2222} \\ E_{3333} \\ E_{1122} \\ E_{1133} \\ E_{2233} \end{bmatrix} \tag{A.11}$$

Solving the above equations then the parameters in Eq. (A.2) will be obtained.

Appendix A.2. The transverse isotropic model

For classical transverse isotropic model, there are 5 independent variables in $\boldsymbol{E}$, which are (supposing $\boldsymbol{e}_3$ is the reference direction of the axisymmetry material)

$$E_{1111}, E_{3333}, E_{1122}, E_{1133}, E_{1313}. \tag{A.12}$$

For peridynamic transverse isotropic model, there are only 3 independent variables in $\boldsymbol{D}$ due to the centrosymmetry of the long range force, which are

$$D_{1111}, D_{3333}, D_{1133} = D_{1313}, \tag{A.13}$$

and D_{1122} depends on the other coefficients. Therefore, Eq. (A.5) means

$$D_{1111} = E_{1111}, D_{3333} = E_{3333}, D_{1133} = E_{1133}. \tag{A.14}$$

Substituting Eq. (A.3) into Eq. (A.4), we have

$$\boldsymbol{D} = a_0\boldsymbol{D}^0 + a_2\boldsymbol{D}^2 + a_4\boldsymbol{D}^4, \tag{A.15}$$

where

$$\boldsymbol{D}^i = \int_{H_\delta(\boldsymbol{x})} \frac{c^1(\|\boldsymbol{\xi}\|)P_i^0(cos(\theta))}{2}\boldsymbol{\xi}\otimes\boldsymbol{\xi}\otimes\boldsymbol{\xi}\otimes\boldsymbol{\xi}\mathrm{d}V_{\boldsymbol{x}'}, \quad i = 0, 2, 4. \tag{A.16}$$

Then, Eq. (A.14) means

$$\begin{bmatrix} D_{1111}^0 & D_{1111}^2 & D_{1111}^4 \\ D_{3333}^0 & D_{3333}^2 & D_{3333}^4 \\ D_{1133}^0 & D_{1133}^2 & D_{1133}^4 \end{bmatrix} \begin{bmatrix} a_0 \\ a_2 \\ a_4 \end{bmatrix} = \begin{bmatrix} E_{1111} \\ E_{3333} \\ E_{1133} \end{bmatrix} \tag{A.17}$$

Solving the above equations then the parameters in Eq. (A.3) will be obtained.

References

[1] A. J. Hey, S. Tansley, K. M. Tolle, et al., The fourth paradigm: data-intensive scientific discovery, Vol. 1, Microsoft Research Redmond, WA, 2009.

[2] D. L. Logan, A first course in the finite element method, Cengage Learning, 2016.

[3] T. Belytschko, W. K. Liu, B. Moran, K. Elkhodary, Nonlinear finite elements for continua and structures, John Wiley & Sons, 2014.

[4] X.-J. Fang, F. Jin, Extended finite element method based on ABAQUS, Engineering Mechanics 24 (7) (2007) 6–10.

[5] E. Lindgaard, B. Bak, J. Glud, J. Sjølund, E. Christensen, A user programmed cohesive zone finite element for ANSYS Mechanical, Engineering Fracture Mechanics 180 (2017) 229–239.

[6] M. A. Msekh, J. M. Sargado, M. Jamshidian, P. M. Areias, T. Rabczuk, Abaqus implementation of phase-field model for brittle fracture, Computational Materials Science 96 (2015) 472–484.

[7] G. Molnár, A. Gravouil, 2D and 3D Abaqus implementation of a robust staggered phase-field solution for modeling brittle fracture, Finite Elements in Analysis and Design 130 (2017) 27–38.

[8] J.-Y. Wu, Y. Huang, Comprehensive implementations of phase-field damage models in Abaqus, Theoretical and Applied Fracture Mechanics 106 (2020) 102440.

[9] S. A. Silling, Reformulation of elasticity theory for discontinuities and long-range forces, Journal of the Mechanics and Physics of Solids 48 (1) (2000) 175–209.

[10] S. A. Silling, M. Epton, O. Weckner, J. Xu, E. Askari, Peridynamic states and constitutive modeling, Journal of Elasticity 88 (2) (2007) 151–184.

[11] X. Chen, M. Gunzburger, Continuous and discontinuous finite element methods for a peridynamics model of mechanics, Computer Methods in Applied Mechanics and Engineering 200 (9-12) (2011) 1237–1250.

[12] Y. Azdoud, F. Han, G. Lubineau, The morphing method as a flexible tool for adaptive local/non-local simulation of static fracture, Computational Mechanics 54 (3) (2014) 711–722.

[13] B. Ren, C. Wu, E. Askari, A 3D discontinuous Galerkin finite element method with the bond-based peridynamics model for dynamic brittle failure analysis, International Journal of Impact Engineering 99 (2017) 14–25.

[14] S. A. Silling, Dynamic fracture modeling with a meshfree peridynamic code, in: Computational Fluid and Solid Mechanics 2003, Elsevier, 2003, pp. 641–644.

[15] S. A. Silling, E. Askari, A meshfree method based on the peridynamic model of solid mechanics, Computers & Structures 83 (17-18) (2005) 1526–1535.

[16] P. Seleson, D. J. Littlewood, Convergence studies in meshfree peridynamic simulations, Computers & Mathematics with Applications 71 (11) (2016) 2432–2448.

[17] C. Diyaroglu, E. Madenci, N. Phan, Peridynamic homogenization of microstructures with orthotropic constituents in a finite element framework, Composite Structures 227 (2019) 111334.

[18] X. Huang, Z. Bie, L. Wang, Y. Jin, X. Liu, G. Su, X. He, Finite element method of bond-based peridynamics and its ABAQUS implementation, Engineering Fracture Mechanics 206 (2019) 408–426.

[19] Y. Bie, Z. Liu, H. Yang, X. Cui, Abaqus implementation of dual peridynamics for brittle fracture, Computer Methods in Applied Mechanics and Engineering 372 (2020) 113398.

[20] R. W. Macek, S. A. Silling, Peridynamics via finite element analysis, Finite Elements in Analysis and Design 43 (15) (2007) 1169–1178.

[21] F. Han, Z. Li, A peridynamics-based finite element method (perifem) for quasi-static fracture analysis, Acta Mechanica Solida Sinica 35 (3) (2022) 446–460.

[22] Z. Li, F. Han, The peridynamics-based finite element method with adaptive continuous/discrete element implementation for fracture simulation (under review).

[23] E. Madenci, E. Oterkus, Peridynamic theory and its applications, Springer, New York, NY, 2014.

[24] F. Bobaru, M. Yang, L. F. Alves, S. A. Silling, E. Askari, J. Xu, Convergence, adaptive refinement, and scaling in 1D peridynamics, International Journal for Numerical Methods in Engineering 77 (6) (2009) 852–877.

[25] G. Lubineau, Y. Azdoud, F. Han, C. Rey, A. Askari, A morphing strategy to couple non-local to local continuum mechanics, Journal of the Mechanics and Physics of Solids 60 (6) (2012) 1088–1102.

[26] Y. Wang, F. Han, G. Lubineau, Strength-induced peridynamic modeling and simulation of fractures in brittle materials, Computer Methods in Applied Mechanics and Engineering 374 (2021) 113558.

[27] H. Yu, S. Li, On energy release rates in peridynamics, Journal of the Mechanics and Physics of Solids 142 (2020) 104024.

[28] F. Han, G. Lubineau, Y. Azdoud, A. Askari, A morphing approach to couple state-based peridynamics with classical continuum mechanics, Computer Methods in Applied Mechanics and Engineering 301 (2016) 336–358.

[29] H. Ren, X. Zhuang, Y. Cai, T. Rabczuk, Dual-horizon peridynamics, International Journal for Numerical Methods in Engineering 108 (12) (2016) 1451–1476.

[30] Dassault Systëmes, Abaqus analysis user's manual (2012).

[31] B. J. Winkler, Traglastuntersuchungen von unbewehrten und bewehrten betonstrukturen auf der grundlage eines objektiven werkstoffgesetzes für beton, Ph.D. thesis, Universität Innsbruck (2001).

[32] M. Nooru-Mohamed, E. Schlangen, J. G. van Mier, Experimental and numerical study on the behavior of concrete subjected to biaxial tension and shear, Advanced Cement Based Materials 1 (1) (1993) 22–37.

[33] T. Ni, M. Zaccariotto, Q.-Z. Zhu, U. Galvanetto, Static solution of crack propagation problems in peridynamics, Computer Methods in Applied Mechanics and Engineering 346 (2019) 126–151.

[34] J.-Y. Wu, Y. Huang, H. Zhou, V. P. Nguyen, Three-dimensional phase-field modeling of mode I+II/III failure in solids, Computer Methods in Applied Mechanics and Engineering 373 (2021) 113537.

[35] D. Brokenshire, A study of torsion fracture test, Ph.D. thesis, Cardiff University (1996).

[36] A. D. Jefferson, B. Barr, T. Bennett, S. Hee, Three dimensional finite element simulations of fracture tests using the craft concrete model, Computers and Concrete, An International Journal 1 (3) (2004) 261–284.

[37] F.-G. BUCHHOLZ, V. Just, H. Richard, Computational simulation and experimental findings of three-dimensional fatigue crack growth in a single-edge notched specimen under torsion loading, Fatigue & Fracture of Engineering Materials & Structures 28 (1-2) (2005) 127–134.

[38] L. Benedetti, M. Cervera, M. Chiumenti, 3D numerical modelling of twisting cracks under bending and torsion of skew notched beams, Engineering Fracture Mechanics 176 (2017) 235–256.

[39] Y. Azdoud, F. Han, G. Lubineau, A morphing framework to couple non-local and local anisotropic continua, International Journal of Solids and Structures 50 (9) (2013) 1332–1341.